

3D Computerized Model for Measuring Strain and Displacement of the Brachial Plexus Following Placement of Reverse Shoulder Prosthesis

TOM VAN HOOFF,^{1*} GERMANO T. GOMES,¹ EMMANUEL AUDENAERT,²
KOENRAAD VERSTRAETE,³ INGRID KERCKAERT,¹ AND KATHARINA D'HERDE¹

¹Department of Human Anatomy, Embryology, Histology and Medical Physics,
University of Ghent, Ghent, Belgium

²Department of Physical Medicine and Rehabilitation,
University of Ghent, Ghent, Belgium

³Department of Radiology, University of Ghent, Ghent, Belgium

ABSTRACT

The aim of the present study was to develop a method for three-dimensional (3D) reconstruction of the brachial plexus to study its morphology and to calculate strain and displacement in relation to changed nerve position. The brachial plexus was finely dissected and injected with contrast medium and leaden markers were implanted into the nerves at predefined places. A reverse shoulder prosthesis was inserted in a cadaveric specimen what induced positional change in the upper limb nerves. Computed tomography (CT) was performed before and after this surgical intervention. The computer assisted image processing package Mimics[®] was used to reconstruct the pre- and postoperative brachial plexus in 3D. The results show that the current interactive model is a realistic and detailed representation of the specimen used, which allows 3D study of the brachial plexus in different configurations. The model estimated strains up to 15.3% and 19.3% for the lateral and the medial root of the median nerve as a consequence of placing a reverse shoulder prosthesis. Furthermore, the model succeeded in calculating the displacement of the brachial plexus by tracking each implanted lead marker. The presented brachial plexus 3D model currently can be used in vitro for cadaver biomechanical analyses of nerve movement to improve diagnosis and treatment of peripheral neuropathies. The model can also be applied to study the exact location of the plexus in unusual upper limb positions like during axillary radiation therapy and it is a potential tool to optimize the approaches of brachial plexus anesthetic blocks. *Anat Rec*, 291:1173–1185, 2008. © 2008 Wiley-Liss, Inc.

Key words: anatomic models; brachial plexus; biomechanics; computer assisted image processing

It is generally accepted that impaired nerve movement can lead to nerve injury (McLellan, 1975; McLellan and Swash, 1976). In the past decades, different techniques, e.g., speckle tracking and Doppler ultrasonography, were developed allowing to infer tissue motion and to estimate strain (Hough et al., 2000; Dilley et al., 2001). Yet to investigate movement of morphological complex nerve structures, there is a need for exact three-dimensional

*Correspondence to: Tom Van Hoof, De Pintelaan 185, 4B3, B-9000 Ghent, Belgium. Fax 32-9240-3809.
E-mail: tom.vanhoof@ugent.be

Received 24 January 2008; Accepted 24 April 2008

DOI 10.1002/ar.20735

Published online 5 June 2008 in Wiley InterScience (www.interscience.wiley.com).

(3D) approaches and computer simulation (Lien et al., 2005). With modern radiographical 2D techniques, it remains difficult to depict detailed anatomy of the brachial plexus and there is few information concerning the topography of the plexus in extraordinary postures of the upper limb. Advanced 3D visualization and measurement techniques are needed to clarify problems in regions with complex anatomic organization. In this study, we present a method to create a 3D model of the cadaveric brachial plexus allowing detailed study of its morphology and its biomechanical behavior after the surgical procedure of placing a reverse shoulder prosthesis.

Abnormal nerve movement can cause peripheral neurological disorders such as thoracic outlet syndrome (TOS) and carpal tunnel syndrome (CTS). Reduced transverse movement of the median nerve has been observed in both subjects with CTS (Nakamichi and Tachibana, 1995; Allmann et al., 1997; Hough et al., 2007) and nonspecific arm pain (Greening et al., 1999, 2001). Julius et al. (2004) found by means of ultrasound measurements, that shoulder protraction restricts median nerve sliding through the shoulder region up to 60%. They conclude that sustained shoulder protraction may place the median nerve at enhanced risk of injury and possibly can cause a neurovascular compromise. Nevertheless, they were unable to establish or visualize the precise cause of the entrapment because of the restrictions of ultrasound measurement techniques when applied to a movement in a complex joint with many different interplaying hard and soft tissues.

Another example is the field of TOS and particularly these forms that are strongly related to poor posture and predisposing morphotype in the absence of anatomical anomalies. Demondion et al. (2000) stated that a complete understanding of the normal relationship between the components of the thoracic outlet and the neurovascular bundle is essential for interpreting signs of compression in TOS. They reported on compression and dynamic modifications of the thoracic outlet in association with postural manoeuvres by means of magnetic resonance imaging (MRI) and color duplex ultrasonography (Demondion et al., 2003, 2006). Patients with TOS had a smaller costoclavicular distance around the brachial plexus after hyperabduction. They also concluded that ultrasonography should not be used solely but as a supplementary technique to computed tomography (CT) or MRI because it does not allow an accurate overview of the thoracic outlet region (Demondion et al., 2003, 2006). The disadvantage of planar CT or MRI is that 2D images only allow interpretation in one plane at the time. Consequently, these studies of Demondion et al., (2000, 2003, 2006) were mainly focused on compression, when stretch (strain) of the brachial plexus may play another important role in the etiology of TOS.

Swift and Nichols (1984) reported on patients with TOS presenting with a droopy shoulder syndrome and suggested that their symptoms resulted from stretching of the brachial plexus. Ide et al. (2003) distinguished two main categories of TOS. They found that 92% of the 150 patients examined, had neuroradiographic evidence of compression of the brachial plexus in the costoclavicular space and 82% had neuroradiographic evidence of stretching the brachial plexus. Even though it concerned a radiologic study, no details were obtained about amount and exact location of the neural stretch in the plexus.

Detailed anatomical descriptions and imaging studies of the brachial plexus with the upper limb and/or cervical spine in an unusual non-neutral posture are scarce. These are of clinical interest for radiotherapists who are mainly concerned about the exact location of the brachial plexus in the "arms up over the head" position required for axillary radiation, in an attempt to increase tissue selectivity and minimize the hazard of radiation-induced brachial plexopathy (Cash et al., 2005). The exact topography of the plexus and its displacement as a consequence of positioning the patient is also of interest to anesthesiologists in search of a safer and more accurate approach for plexus block anesthesia.

It is generally known that 3D models serve better for anatomical perception of complex structures, when compared with classic plane views. In 2D radiological sections it is up to the viewer to mentally reconstruct the structures; the quality of this process depends on the power of the observer's imagination (Tomandl et al., 2001; Naraghi et al., 2004; Spinner et al., 2006). Therefore, there is need for 3D models which should allow quantitative interpretation of anatomical and biomechanical aspects of the entire plexus in all three dimensions. The purpose of the present research is to develop a method for 3D reconstruction of the brachial plexus to study its morphology in different postures and to measure strain (elongation) and displacement of the plexus caused by procedures influencing the upper limb nerve position, in this study realized by placing a reverse shoulder prosthesis.

METHODS

Subjects

Initially, we used a specimen (male, 69 years) embalmed according to the Thiel method (Thiel, 1992) because it preserves the cadaver without stiffening which represents a major advantage in a biomechanical study. However, tissue solidity proved to be insufficient to sustain properly the surgical procedure of prosthesis insertion. Therefore the only remaining purpose of that cadaver was to elaborate the methodology: we tested the procedure of identifying the different components of the plexus on CT scans after subepineural injection of contrast medium and the feasibility to mark fixed points of the plexus by grafting of lead markers.

A second cadaver (female, 94 years; time between embalming and use: 3 months) embalmed according to our routine procedure (De Maeseneer et al., 2003) was then used for the complete process of brachial plexus preparation, segmentation, 3D reconstruction, prosthesis placement, and measurement.

Procedure

The brachial plexus was carefully dissected from its passage through the interscalene triangle up to the proximal part of the peripheral nerves and local topography was maintained as much as possible. Dissection was continued until all parts were accessible with an injection needle. The clavicle and pectoralis minor muscle were preserved, the pectoralis major muscle was sectioned at its tendon of insertion and later on reinserted before skin closure.

The brachial plexus was injected with a mixture iodine contrast (Visipaque®) with 33% glycerin and

0.075% toluidine blue (Pfrrmann et al., 2001; Feigl et al., 2006). Glycerin increases the viscosity of the mixture (Pfrrmann et al., 2001), the addition of the toluidine blue allows a visual control over dispersion and possible leakage of the mixture. The needle (Terumo[®] needle 0.45 × 23 mm) was inserted under the epineurium (Demondion et al., 2005) of the nervous tissue, and the solution was injected with mild pressure until leakage occurred at the injection site or at spots further away along the nerve segment. The injection sites were distributed along the entire course of the brachial plexus with a mean intermediate distance of approximately 3 cm, depending on the absorbing capacity of the regarding segment.

Subsequently 16 lead beads (lead [Pb] fishing weights, Dinsmores[®] ∅ 3 mm) were implanted into the nerves at predefined places; start of the divisions (3), start of the cords (2), start of the peripheral nerves (4), peripheral nerves at mid-humeral level (3), peripheral nerves at elbow level (3), and one at the end of the axillary nerve.

After the first session of CT scanning (see below) the specimen returned to the cadaver lab and a plastic replica of a reverse shoulder prosthesis was inserted followed by re-injection of the plexus with the same solution. The reverse shoulder prosthesis was placed according to the guidelines of the American Academy of Orthopaedic Surgeons (Matsen et al., 2007). Subsequently, the specimen was scanned with the upper limb in a different position as a consequence of the surgical intervention, that is, insertion of the reverse shoulder prosthesis, further referred to as postoperative. The initial CT scans taken before the surgical intervention and the results originating from it, will be referred to as preoperative.

It should be stressed that this study was not focused on the shoulder prosthesis itself: Rather the initial concept of measuring alterations in nerve position was subjected to a clinically relevant situation, that is, surgical procedure of placing a reverse shoulder prosthesis to develop a generally applicable 3D model for estimating displacement and strain of the brachial plexus.

CT Scanning

The preoperative and postoperative specimens were studied by a helical CT scan (Siemens/ volume zoom). Scanning parameters were 120 KV, 165 mas, slice increment 1 mm, field of view 480 mm, and 512 × 512 pixels (0.938 mm pixel size).

The shoulder of the specimen was positioned in adduction internal rotation and the elbow in approximately 90° flexion. The cervical spine was positioned in neutral position and both wrists were placed and strapped down on the lower abdomen.

The CT images of the first and the second session were uploaded separately into a software package that can import any 2D stack of images (e.g., CT and MRI) and allows 3D reconstruction. In the present study Mimics[®] (Materialise N.V., Heverlee, Belgium) was used for visualization and segmentation of CT images and 3D rendering of the brachial plexus with a direct link to biomechanical analysis of nerve strain (elongation) and displacement.

Thresholding was the first action performed to create a segmentation mask. We selected the region of interest,

that is, brachial plexus with contrast, by defining its specific range of gray values. Subsequently, we performed a “dynamic region growing,” a procedure that segments objects based on the connectivity of gray values in a certain gray value range. This procedure allows for segmentation of nerves in CT images. This approach was repeated for all bones of the upper quadrant and the lead markers implanted in the nerves. Further manual adjusting was performed to eliminate errors originating from the semi automatic reconstruction phase.

Measurements

In Mimics, each lead marker in the 3D model was indicated by a virtual tag by means of the “measure and analyze” tool. Virtual tags were also placed on predefined positions of each part of the brachial plexus (Fig. 1A,B). This procedure was repeated for the pre- and the postoperative project.

Thereafter the virtual tags were exported as text files which allowed to obtain the corresponding coordinates (x,y,z) of these points, which were set relative to the coordinate system inherent to the Mimics software program itself. The text files containing the coordinates were then imported into Matlab[®] (Mathworks, Inc., Natick, MA) where a customized algorithm calculated the best fitting curve (i.e., smooth spline) in a way that it approached the real path of the nerves as much as possible.

The distance between two successive lead markers calculated along the path of the nerve produced the real length of that particular segment. The shortest distance (i.e., straight line) between two successive lead markers was also calculated and is referred to as vector length.

In Matlab, the different coordinate system of the postoperative brachial plexus was transformed (i.e., translated and rotated) into the same coordinate system of the preoperative brachial plexus. To achieve that, supplementary virtual tags were placed at each intervertebral foramina (C5–T1) and at the bifurcation of the xiphoid process, identically for both the pre- and the postoperative project. Matlab then calculated the rigid body transformation matrix providing the best fit, in a least squares sense, between these pairs of reference points and subsequently transformed the postoperative into the preoperative project.

This alignment was performed to allow calculation of the displacement of each lead marker inside the brachial plexus as a result of positional change of the neural tissue caused by placing the reverse prosthesis. This displacement is calculated as the shortest distance (straight line) between the pre- and postoperative position of the marker.

The transformation was also performed in Mimics to visualize the pre- and postoperative plexus in the same coordinate system. The reference points of two intervertebral foramina (C5 and C8) and the xiphoid process bifurcation were incorporated in the mask of the brachial plexus followed by a recalculation of the 3D object. The marking of these bony reference points resulted in the appearance of three additional points in the 3D model representing these specific anatomical locations. This procedure was performed for both the pre- and postoperative project. Then the postoperative 3D object was saved in the STL format (Stereolithography, simple

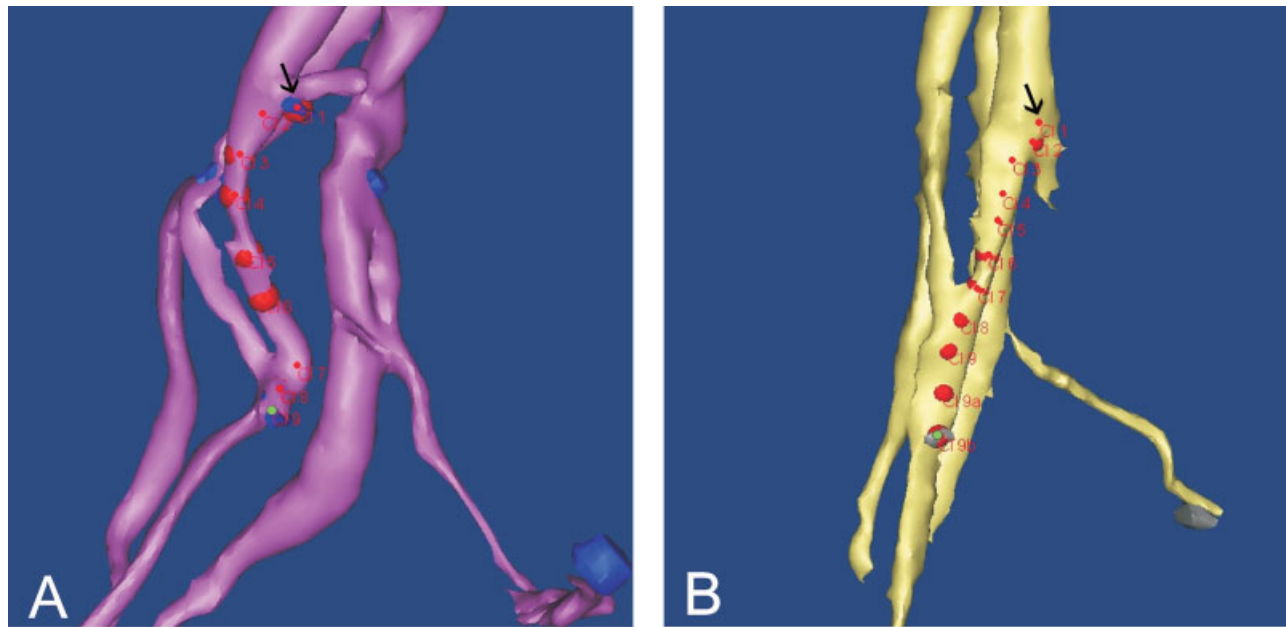


Fig. 1. Illustration of the placing of virtual tags (red dots) in the lateral root of the median nerve. **A:** The preoperative plexus in purple; the blue beads represent the lead markers; this image clearly demonstrates that the initial and final virtual tags coincide respectively with the lead markers that indicate the start and the end of the regarding nerve segment (the initial virtual tag is indicated by the black arrow;

the final virtual tag is represented by the little green dot in the blue lead marker indicating the end of the lateral root of median nerve). **B:** The postoperative plexus in yellow; the gray beads represent the lead markers; the little green dot indicates the final virtual tag coinciding with the lead marker distally delimiting the nerve segment; the initial virtual tag is also indicated by the black arrow.

output format of Computer Aided Design systems) and imported into the preoperative project where it became visible but not aligned with the preoperative plexus. Using the “point registration” tool in Mimics, the corresponding reference points were selected and aligned in a manner similar to the procedure in Matlab.

Data Collection

We measured real length of each nerve segment between subsequent lead markers, and vector length as the straight distance between the lead markers. The real length of each nerve segment in the preoperative project is assumed as the normal not-elongated reference length. The formula $(l_{rPost} - l_{rPre}) / l_{rPre} \times 100\%$ allows to calculate strain (or shortening) of a nerve segment by substituting its pre- and postoperative real length (respectively, l_{rPre} and l_{rPost}).

The amount of coiling or curve was estimated by the ratio of vector length to real length through the formula $(l_v - l_r) / l_r \times 100\%$ with l_v as the vector length and l_r as the real length, resulting in a negative value. No coiling occurs when both lengths equal (0%) and when for example the vector length is 4/5 of the real length, 20% of coiling is expressed by the formula as -20% . If postoperatively the real length of the nerve segment is increased (strain), this inevitably implicates that the coil of the neural tissue is completely taken up. If in this situation still a negative ratio is obtained $[(l_v - l_r) / l_r \times 100\%]$, this means that the nerve follows a curved course what is also characterized by the real length being longer than the vector length.

Finally, the absolute displacement of one and the same lead marker between the pre- and postoperative situation was also calculated as a vector length (shortest distance).

The mean error ($error_1$) of placing the virtual tags in the lead markers and the circular 95% confidence interval were calculated. This procedure had to be considered two times because length is determined between two virtual markers: we used the upper limit as a critical value for the differences in length of the nerve segments ($2 \text{ error}_1 + 1.96 (\text{SE}_1^2 + \text{SE}_2^2)^{1/2} = 0.87 \text{ mm}$). Differences smaller than 0.87 mm were attributed to random noise and are below the resolution of this method and are not considered for the strain calculation.

To assess significant displacement of each lead marker between the pre- and postoperative situation, a second critical value was calculated as the summation of the first error ($error_1$) of placing the virtual tags and a second error ($error_2$) inherent in the transformation process of the coordinate system of the postoperative plexus. This resulted in 1.89 mm ($2 \text{ error}_1 + \text{error}_2 + 1.96 (\text{SE}_1^2 + \text{SE}_2^2)^{1/2} = 1.89 \text{ mm}$); the distance between the pre- and postoperative position of a particular lead marker (in the same coordinate system) has to exceed this critical value to be determined as a significant displacement.

RESULTS

Figure 2A–D illustrates that the anatomical details of the cadaveric brachial plexus are also depicted in the reconstructed plexus. Figure 2B shows the crossing of the lateral root of the median nerve over the axillary ar-

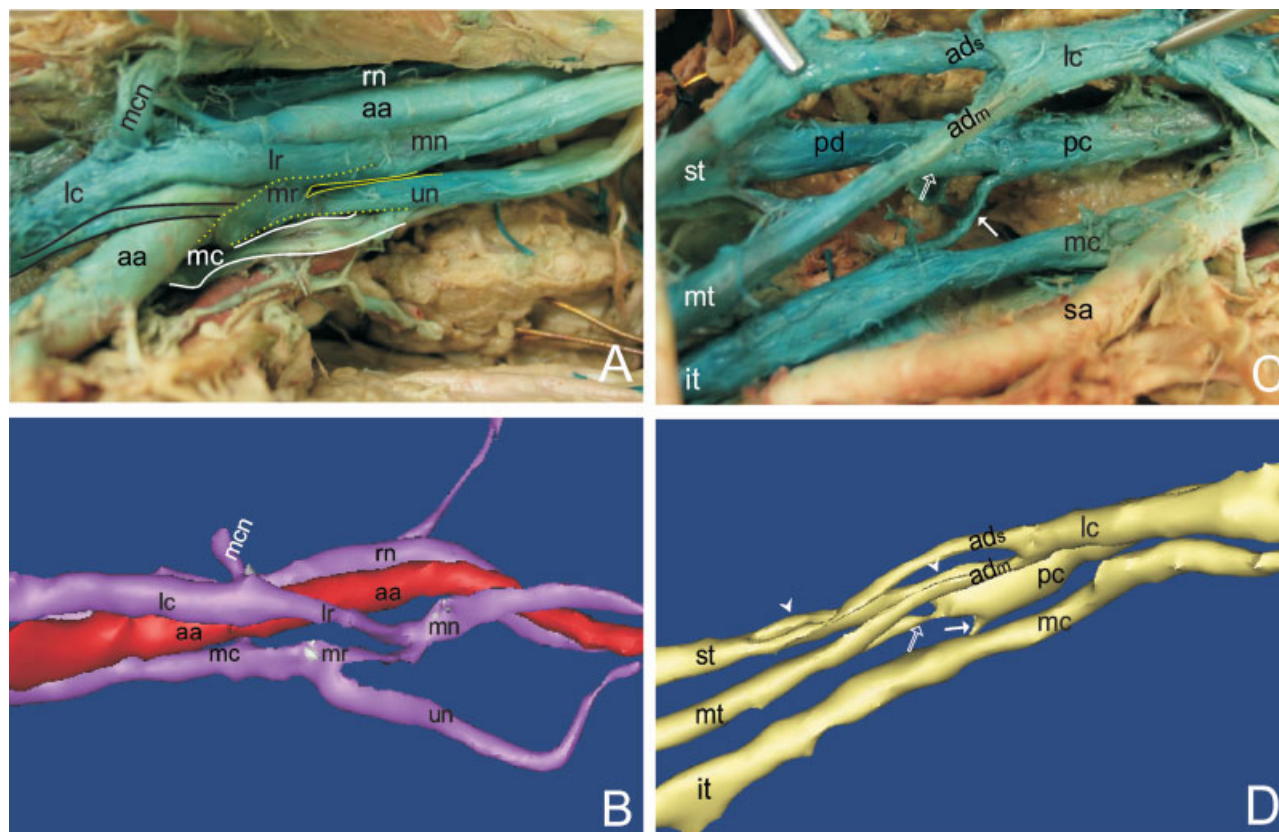


Fig. 2. **A–D:** Comparison between the dissected brachial plexus (A,C) and the 3D reconstructed plexus (B,D) shows structural conformity: A,B infraclavicular level and C,D level of the divisions. A,B: aa, axillary artery; lc, lateral cord; mc, medial cord; lr, lateral root of the median nerve; mr, medial root of the median nerve; mn, median nerve; mcn, musculocutaneous nerve; rn, radial nerve; un, ulnar nerve. A: Area between yellow dots represents common trunk of the medial cord bifurcating into medial root of median nerve above double yellow line and ulnar nerve below; area between white lines represents medial cutaneous nerve of the arm and forearm; area between black

lines represents surnumerary lateral root of median nerve. C,D: st, superior trunk; mt, middle trunk; it, inferior trunk; ads, anterior division of superior trunk; adm, anterior division of middle trunk; pd, posterior division of superior trunk; lc, lateral cord; mc, medial cord; pc, posterior cord; sa, subclavian artery. C: White open arrow, posterior division of middle trunk, white arrow, posterior division of inferior trunk. D: white arrow heads, posterior division of superior trunk; white open arrow, posterior division of middle trunk; white arrow, posterior division of inferior trunk. The subclavian artery is left out of the reconstruction for illustrative reasons.

tery and the subsequent drop posteriorly, which is clearly visible in corresponding cadaveric picture (Fig. 2A).

Of interest, the cadaveric brachial plexus displays an anatomical variant: there is a second smaller lateral root of the median nerve—area between black lines (Fig. 2A)—that parallels the original one medially and also crosses the axillary artery. The medial cutaneous nerves of the arm and the forearm are situated between both white lines (Fig. 2A). These cutaneous nerves and the surnumerary lateral root of the median nerve (Fig. 2A) were not injected with contrast fluid and as a consequence were not depicted in the 3D model (Fig. 2B). The fact that these noninjected nervous structures, as well as the axillary artery, appear pale blue is due to diffusion of contrast fluid. It should be noted that this dissection, to illustrate the morphology of the plexus in detail, was performed several days after the scanning procedure.

To improve identification of the different components of the plexus in Figure 2C, the anterior division of the

superior trunk and the lateral cord were lifted, exposing the posterior division of the superior trunk. The dissection in the axilla (Fig. 2A) could only be performed if the shoulder was slightly externally rotated and abducted as compared to its position during scanning. The different positioning of the cadaver during dissection and scanning (shoulder slightly adducted and internally rotated) can explain the minor positional divergencies between the original cadaveric and the reconstructed plexus. Notably, there is the increased curvature of the ulnar nerve and the changed orientation of the musculocutaneous nerve (Fig. 2B).

Measurements

Figures 3 and 4 illustrate the reconstructed plexus in relation to the cervical spine, the first rib, the bones of the shoulder girdle, and the subclavian/axillary artery. Figure 5A shows the distal movement of the postoperative humerus (light gray). The postoperative humerus is slightly flexed posteriorly (retroflexed) and externally

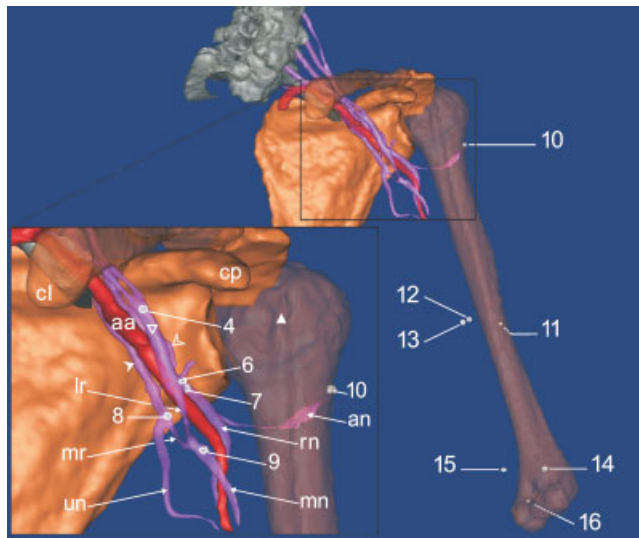


Fig. 3. Preoperative: Overview of the cervical spine and posterior part of the first rib (gray); clavicle (cl), scapula and the semi-transparent humerus (brown); brachial plexus (purple) and axillary artery (aa) (red). Preoperative markers (light gray) of the nonreconstructed peripheral nerves at mid-humeral level: 11, marker of radial nerve behind humerus; 12, marker of median nerve; 13, marker of ulnar nerve and at "near elbow" level: 14, marker of radial nerve; 15, marker of median nerve; 16, marker of ulnar nerve behind the medial epicondyle. Median nerve from marker 9 to 12; ulnar nerve from marker 8 to 13; radial nerve from marker 7 to 11: the nonreconstructed parts of these nerves (distal from inset) extend from the end of the visible peripheral nerve (purple) to the corresponding mid-humeral marker represented in the model by an imaginary straight line. Median nerve II, ulnar nerve II and radial nerve II: imaginary straight lines connecting respectively markers 12–15, 13–16 and 11–14 according to the segments used in Table 1. Inset shows the preoperative brachial plexus (purple) and axillary artery (aa) in detail. Notice the coiled appearance of the brachial plexus distal from the coracoid process (cp). cl, clavicle; contours of posterior part of first rib (dark gray) appear in the sternal facet of the semi-transparent clavicle just below aa; lr, lateral root of the median nerve; mr, medial root of the median nerve; mn, median nerve; un, ulnar nerve; rn, radial nerve; an, axillary nerve with gray marker 10 at the end behind humerus; open white inverted triangle, lateral cord; full white arrowhead, medial cord; open white arrowhead, posterior cord; 6, marker at the end of lateral cord indicating bifurcation of lr and the musculocutaneous nerve (stump with craniolateral orientation); 8, marker at the end of medial cord indicating bifurcation of mr and un; 9, marker indicating the start of mn; full white triangle, bicipital groove of humerus flanked medially by the lesser tubercle and laterally by the greater tubercle.

rotated in comparison to the preoperative situation (Fig. 5A–C).

In this section, only the results concerning the distal part of the plexus are described. The results for the proximal part are summarized in Table 3 and can be found in the appendix. Figure 6A,B provides an overview of the location of the different lead markers dividing the brachial plexus in different nerve segments.

Figures 3 and 7 show the convoluted course for both the lateral and the medial root of the median nerve preoperatively. This is in accordance with the corresponding ratios determining -19.3% coil for the lateral and -17.1% coil for the medial root as demonstrated in Table 1.

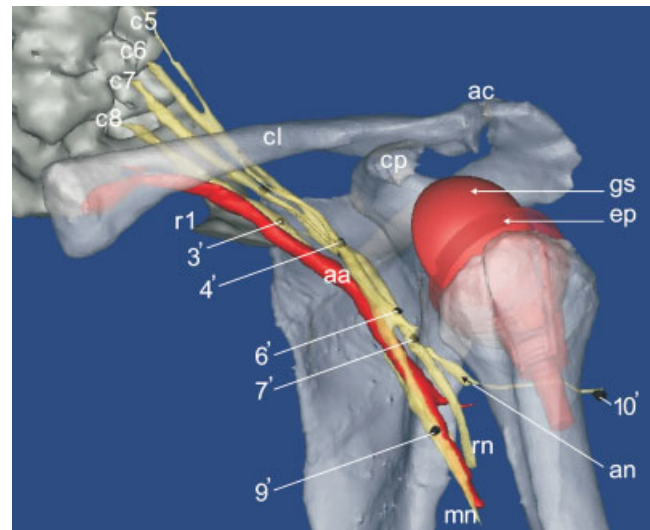


Fig. 4. Postoperative: Overview of the cervical spine and posterior part of the first rib (r1) (dark gray); clavicle (cl), scapula and humerus (light gray), brachial plexus (yellow) and axillary artery (aa) (red). Notice the reverse shoulder prosthesis with the glenosphere (gs) inserted into the glenoid cavity and the epiphysis (ep) part inserted into the humeral shaft. Also notice the straightened out appearance of the postoperative brachial plexus in comparison to Figure 3 preoperatively. c5–c8, roots c5–c8; mn, median nerve; rn, radial nerve; an, axillary nerve; cp, coracoid process; ac, acromioclavicular joint; 3', marker in inferior trunk at bifurcation of posterior division and medial cord; 4', marker at start of lateral cord; 6', marker at the end of lateral cord indicating bifurcation of lateral root median nerve and the musculocutaneous nerve (notice the changed orientation of the latter); 7', marker at end of posterior cord indicating bifurcation in "an" and "rn"; 9', marker at start of median nerve; 10', marker at end of axillary nerve.

In the lateral root of the median nerve, 15.3% strain is recorded postoperatively due to the distal displacement of the humerus. In the medial root of the median nerve, strain up to 19.3% is found (Table 1; Fig. 7). Accordingly, Figures 4 and 7 show that postoperatively this convoluted course is completely straightened out. Despite this, Table 1 still indicates negative ratio values (nerve topology) for the regarding segments postoperatively, to be precise -7.3% for the lateral and -7.5% for the medial root. These negative values, cannot implicate coil because the concerning parts are strained meaning that the coil inevitably is taken up. Figure 7 illustrates postoperatively (in yellow) the curved course (representing real length) of the lateral and medial root of the median nerve in comparison to the straight vector length which explains these negative values. The real length of the lateral root of the median nerve is demonstrated by the light blue dotted line along the curved course of this nerve segment (extending) from marker 6 to 9 in comparison with the interrupted red line representing the vector length as the straight distance between the same markers (Fig. 7).

The preoperative median nerve (segment from marker 9 to 12; Fig. 3) was found to be coiled -2.2% , and after the surgical procedure, it was strained for 2.9% (Table 1). Postoperatively, this nerve segment is not curved but just follows a straight course as indicated by the 0% ratio, which is a result of the fact that the real length

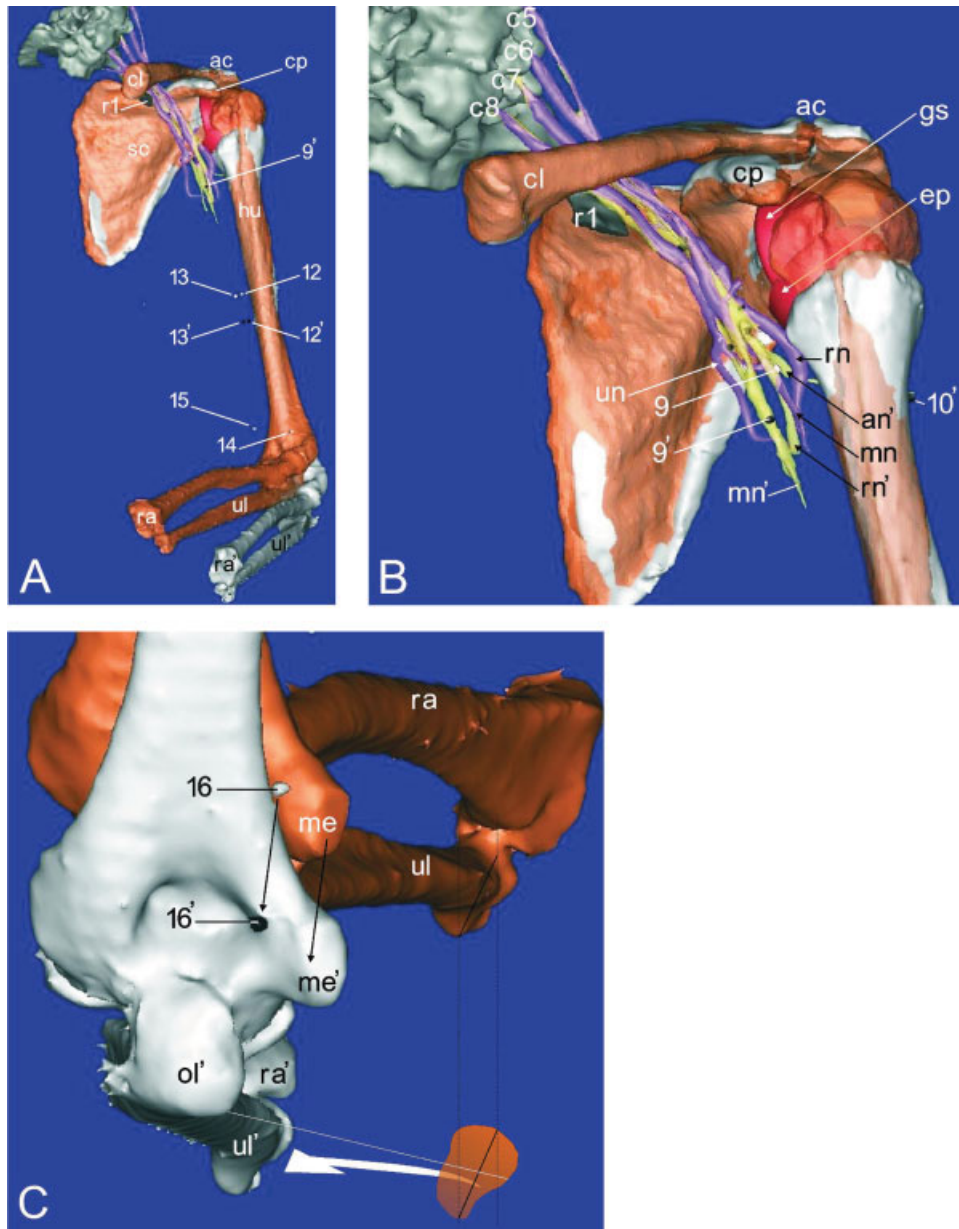


Fig. 5. **A:** Overview of postoperative reconstruction transformed into the coordinate system of preoperative reconstruction. Purple plexus and brown clavicle, scapula, humerus, radius and ulna represent the preoperative project (preop.); yellow plexus and the light gray bones represent the postoperative project (postop.). The cervical spine and the posterior part of the first rib (dark gray) are identically for both projects. White markers of the medial (12) and ulnar nerve (13) at mid-humeral level preop. are distally displaced according the distal shift of the humerus following surgery: 12' and 13', black markers respectively of medial and ulnar nerve at mid-humeral level postop.; 9', marker at the origin of the median nerve in postop. plexus; 14 and 15, markers respectively of radial and median nerve at "near elbow" level preop. **B:** Close-up of shoulder girdle showing the pre- and the postoperative plexus together allowing to appreciate the alterations in the postoperative situation. The postoperative clavicle (cl) in light gray remained stable with only a small elevation of the acromioclavicular joint (ac); notice the slight elevation of the postoperative (light gray) coracoid process (cp) and acromion medial from the ac-joint and the inward kipping of the medial border and the inferior angle of the postoperative (light gray) scapula; also notice the distal shift and the posterior

flexion (retroflexion) of the postoperative humerus (light gray) and the straight appearance of the postoperative plexus. c5–c8, roots cervical 5–8; gs, glenosphere and ep, epiphysse both part of the reverse shoulder prosthesis; mn and mn', median nerve pre- and postoperative e; un, ulnar nerve preoperative; an', axillary nerve postop.; 9 and 9' markers at origin of medial nerve preoperative (white) and postop. (black); 10', marker indicating the end of the postoperative axillary nerve passing behind the humerus. **C:** Posterior view of the elbow joint illustrating the distal shift of the humerus. Left black arrow illustrates the displacement of the lead marker in the ulnar nerve between preoperative (16, gray) and postoperative (16', black). The right black arrow illustrates the displacement of the medial epicondyle (me) between pre- and postoperative (me'). This image also shows the external rotation (white arrow) of the postoperative humerus (light gray) in comparison with the preoperative orientation of the humerus (brown). sc, scapula; cp, coracoid process; cl, clavicle; ac, acromioclavicular joint; r1, first rib; hu, humerus; ra and ra', pre- and postop. radius; ul and ul', pre- and postoperative ulna; ol', olecranon postop.

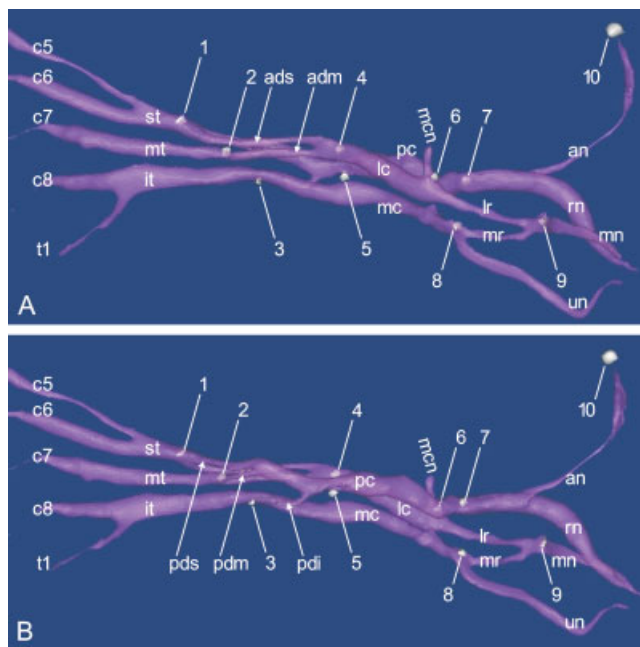


Fig. 6. Both figures indicate the different parts of the left preoperative brachial plexus and the exact location and numbering of each lead marker. **A:** Anterior view. **B:** Posterior view of the left brachial plexus which is mirrored to align roots at the same site. c5–c8, roots cervical 5–8; t1, root thoracic 1; st, superior trunk; mt, middle trunk; it, inferior trunk; ads, anterior division of superior trunk; adm, anterior division of middle trunk; pds, posterior division of “st”; pdm, posterior division of “mt”; pdi, posterior division of “it”; pc, posterior cord; lc, lateral cord; mc, medial cord; mcn, musculocutaneous nerve; lr, lateral root of median nerve; mr, medial root of median nerve; mn, median nerve; an, axillary nerve; rn, radial nerve; un, ulnar nerve; 1, lead marker in the superior trunk at bifurcation in “ads” and “pds”; 2, lead marker in middle trunk at bifurcation in “adm” and “pdm”; 3, lead marker in inferior trunk at bifurcation in “pdi” and start of “mc”; 4, lead marker at the start of “lc”; 5, lead marker at the start of “pc”; 6, lead marker at end of “lc” bifurcating into “mcn” and “lr” (in B this marker is visible at its proper location right through the semi-transparent posterior cord); 7, lead marker at end of posterior cord bifurcating into “an” and “rn”; 8, lead marker at end of medial cord bifurcating into “mr” and “un”; 9, lead marker at start of peripheral median nerve; 10, lead marker at end of axillary nerve.

equals the vector length; that is, the difference between both does not exceed the critical value of 0.87 mm (marked in Table 1 as §).

The distal part of the median nerve, ending in mid-humeral lead marker 12 is not visible in the model (see Figs. 3, 5A: illustrating the end of the reconstructed pre- and postoperative plexus and showing at mid-humeral level marker 12 (gray, preoperative) and 12' (black, postoperative), indicating the end of the median nerve segment, defined in Table 1 as “Med N”). This distal part was not reconstructed because it was beyond the boundaries of the area injected with contrast fluid. These distal parts are represented in the model by imaginary straight lines connecting the ends of the reconstructed major peripheral nerves to the corresponding mid-humeral markers (Fig. 3). The final segments of the peripheral nerves (indicated with II in Table 1) are represented

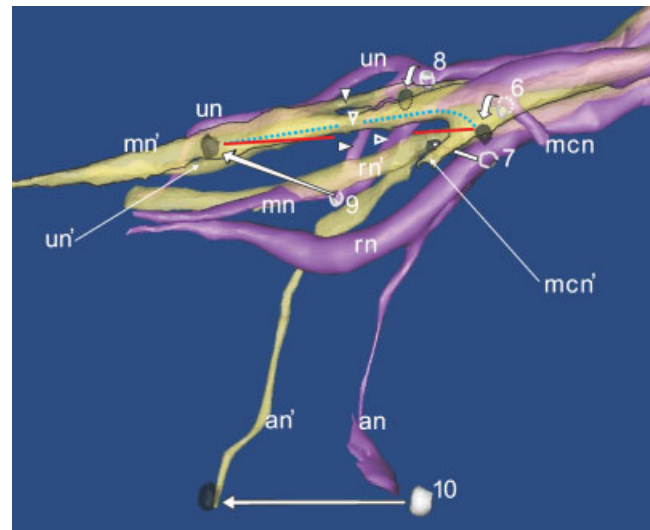


Fig. 7. Illustration of pre- and postoperative brachial plexus. The preoperative plexus (preop.) is opaque purple and the markers are outlined in light gray color. The postoperative plexus (postop.) is represented in semitransparent yellow with black markers. 6 and 8, markers indicating the origin of respectively the lateral and medial root of the median nerve; white triangles indicate the lateral (open) and medial root (full) of the median nerve: inverted triangles for postop.; horizontally orientated triangles for preop.; notice coiled appearance of the roots preop.; 7, marker at the end of the posterior cord with bifurcation into radial and axillary nerve; 9, marker at the origin of the median nerve; 10, marker at end of axillary nerve. Black outlined white arrows show the displacement (see Table 2) of one and the same marker between the pre- and postop. situation: the curved arrows show the displacement of markers 6 and 8; notice the large displacement of marker 9 and the corresponding stretched out appearance (see Table 1 for strain) of the lateral and medial root of the median nerve; also notice the large displacement of marker 10 at the end of the axillary nerve and the medio-distal displacement of marker 7 at the end of the posterior cord. The light blue dotted line connects marker 6 to 9 along the course of the lateral root of the median nerve thereby illustrating the “real length” of the regarding nerve segment. The red interrupted line connects marker 6 to 9 through a straight line (shortest distance) representing the “vector length” (interrupted to show preop. roots of median nerve). mn and mn', median nerve pre- and postop.; un and un', ulnar nerve pre- and postop.; rn and rn', radial nerve pre- and postop.; an and an', axillary nerve pre- and postop.; mcn and mcn', musculocutaneous nerve pre- and postop.

by imaginary straight lines connecting the mid-humeral markers to the corresponding “near elbow joint” markers (Fig. 3).

As shown in Table 1, strain decreases in these final segments of the peripheral nerves. Because these nerve segments are not reconstructed, they are only represented by the vector length (imaginary straight line) between their successive markers (Fig. 3). Consequently, the ratio $(l_v - l_r)/l_r \times 100\%$ could not be calculated, only the amount of strain is presented in Table 1.

Strain is expressed for each nerve segment separately, as shown in Table 1. If strain is expressed in relation to the total “real length” of a bigger part of the nerve (i.e., from origin to elbow), mean values are found as for example 3.5% strain for the median nerve from marker 6 or 8 to 15, which clearly illustrate the heterogeneous distribution of strain along the different nerve segments (Table 1).

TABLE 1. Real length and vector length of each nerve segment, pre- and postoperatively, determine the biomechanical features for the distal part of the brachial plexus^a

Nerve segment	v. Length (l_v) (mm)	r. Length (l_r) (mm)	Nerve topology ($(l_v - l_r)/l_r \times 100\%$)		Calculation of strain ($(l_{rPost} - l_{rPre})/l_{rPre} \times 100\%$)	
LRMN pre	29.54	36.59	-19.26	Coiled	15.28	Strained
LRMN post	39.10	42.18	-7.30	Curved		
MRMN pre	21.68	26.15	-17.11	Coiled	19.26	Strained
MRMN post	28.85	31.19	-7.49	Curved		
Med N pre	109.17	111.66	-2.23	Coiled	2.94	Strained
Med N post	114.53	114.94	-0.35 [§]	—		
Rad N pre	144.49	152.75	-5.41	Coiled	6.25	Strained
Rad N post	160.22	162.29	-1.28	Curved		
Uln N pre	124.19	140.62	-11.68	Coiled	3.37	Strained
Uln N post	142.15	145.37	-2.21	Curved		
Ax N pre	53.20	70.91	-24.97	Curved	-10.51	Shortened [#]
Ax N post	59.10	63.46	-6.87	Coiled		
Med N II pre	111.95	(111.95)	—	—	0.29 [§]	—
Med N II post	112.27	(112.27)	—	—		
Rad N II pre	119.01	(119.01)	—	—	0.77	Strained
Rad N II post	119.92	(119.92)	—	—		
Uln N II pre	137.27	(137.27)	—	—	1.01	Strained
Uln N II post	138.65	(138.65)	—	—		

^aThe ratio of the pre- and postoperative real lengths (l_{rPre} and l_{rPost}) determines the amount of strain of a particular nerve segment of the distal brachial plexus. This percentage interpreted together with the ratio of the real length and the vector length (l_r and l_v) provides information concerning the topology of the nerve segment. pre, preoperative plexus; post, postoperative plexus; v. Length, vector length, shortest distance between both markers demarcating the nerve segment; r. Length, real length measured along the nerve course; Pb, lead marker; Rad N, radial nerve (Pb 7–11); LRMN, lateral root of median nerve; MRMN, medial root of median nerve; N Med, median nerve (Pb 9–12); Ax N, axillary nerve; Uln N, ulnar nerve (Pb 8–13); Med N II, most distal median nerve segment (Pb 12–15); Uln N II, most distal ulnar nerve segment (Pb 13–16); Rad N II, most distal radial nerve segment (Pb 11–14). For the last three segments, only the vector length is measured and accepted as real length – and put in brackets in order to calculate strain. The [§] indicates that the difference between both lengths does not exceed the critical level of 0.87 mm, which means that it can be attributed to the error of the measurement procedure with 95% confidence. The [#] refers to the part of the text where Figure 8A,B is discussed explaining this unexpected finding.

Finally some interesting results are found for the axillary nerve. Figure 8A shows clearly that the preoperative negative ratio [$(l_v - l_r)/l_r \times 100$] of -24.9%, presented in Table 1, represents a curved course (white dotted line). Postoperatively, the axillary nerve unwinds and the real length shortens for -10.5% resulting in a coiled course (black dotted line) for almost -7% as illustrated in Figure 8B (Table 1). Notwithstanding this result, the vector length of the axillary nerve (straight distance between 7' and 10') is increased with 5.9 mm in comparison to the preoperative vector length (Table 1; Fig. 8A,B). Also notice the increased downward slope of the black line postoperative along, which the vector length is measured (Fig. 8B).

DISCUSSION

Figure 2A–D illustrates that the reconstructed brachial plexus is in structural conformity with the cadaveric plexus. All different parts of the plexus from the roots over the trunks and the divisions to the cords ending in the peripheral nerves, which were injected with contrast fluid are clearly depicted in the model. The interactive software allows different view angles, colorings and magnifications which means a considerable advantage in unraveling and describing the complex organization of the brachial plexus. The current 3D model provides the first estimates of brachial plexus nerve strain following insertion of a reverse shoulder prosthesis in a cadaver specimen. In addition, the model suggests which areas of the plexus may be at greatest risk of strain induced

injury. Maximal postoperative strain was found in the medial root (19.3%) and the lateral root (15.3%) of the median nerve. The most significant displacement occurred in lead markers 9 to 16, which moved distally in harmony with the humeral shift as a consequence of insertion of the prosthesis (Table 2). The results of the present study demonstrate that the 3D model allows detailed study of the brachial plexus in different postures and that the model is suitable for measuring biomechanical alterations of the plexus as a consequence of the surgical procedure of reverse shoulder prosthesis placement.

Anatomical studies based on cadaver dissection only can of course also provide detailed insight into the morphology of the brachial plexus (Pandey and Shukla, 2007; Singhal et al., 2007). Cadaver studies also have identified ranges and directions of nerve movement and mechanical strain in nerves in different positions of the upper limb (Millesi et al., 1990; Kleinrensink et al., 1995, 2000; Wright et al., 1996). A major disadvantage of cadaver studies is that measurements of mechanical events need to be performed on the specimen itself, which is only possible after profound dissection freeing the nerve from its surrounding attachments which in turn may affect local biomechanics. Furthermore, that approach permits only to focus one structure or event at the time in contrast to the 3D interactive models. Additional weaknesses of cadaver studies are the limited availability of different view angles and the fact that change of the specimen's posture may inadvertently compromise the visibility and topology of the structures of interest.

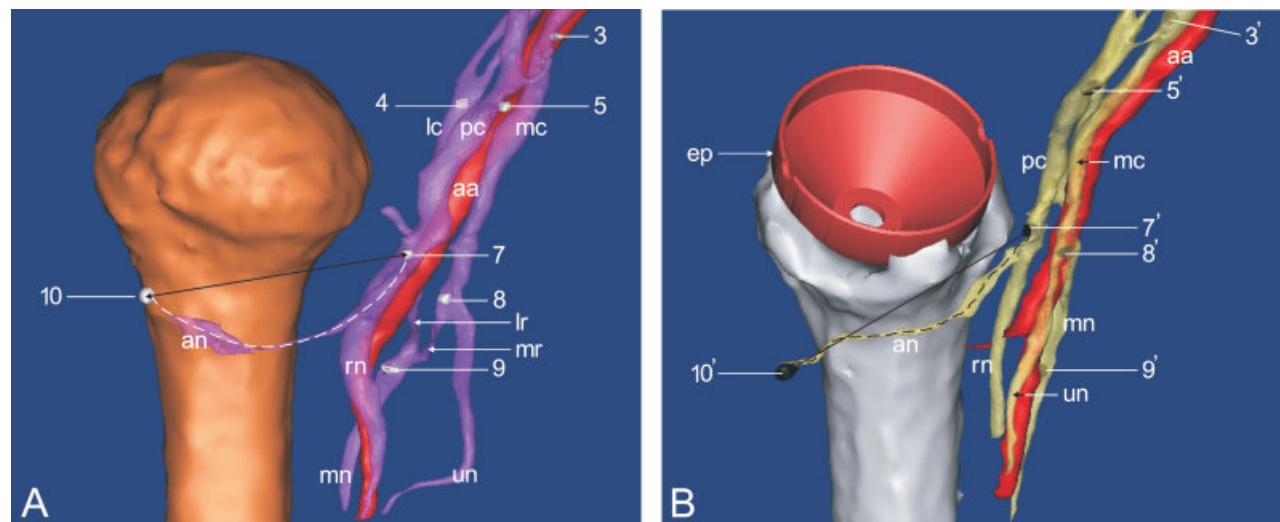


Fig. 8. Posterior view of axillary nerve wrapping around the surgical neck of the humerus. **A:** The curved course of the axillary nerve preoperative (brachial plexus in purple, preop.). The straight line (black) between light gray markers 7 and 10, indicating the start and end of the axillary nerve, represents the vector length. The white dotted line along the course of the axillary nerve represents the real length. **B:** The coiled course of the axillary nerve and marker 10' moved away from the humerus postoperative (brachial plexus in yellow, postop.). The straight line (black) between black markers 7' and 10', indicating the start and end of the axillary nerve postop., represents the vector length. The black dotted line along the course of the

axillary nerve represents the real length. aa, axillary artery; mc, medial cord; lc, lateral cord; pc, posterior cord; lr, lateral root of the median nerve; mr, medial root of the median nerve; mn, median nerve; un, ulnar nerve; rn, radial nerve; an, axillary nerve; ep, epiphys of reverse shoulder prosthesis; 3 and 3', marker at end of inferior trunk pre- and postop.; 4, marker at start of lateral cord; 5 and 5', marker at start of posterior cord pre- and postop.; 7 and 7', marker at end of posterior cord bifurcating into "an" and "rn" pre- and postop.; 8 and 8', marker at start of medial root of median nerve pre- and postoperative; 9 and 9', marker at start of median nerve pre- and postoperative; 10 and 10' marker at end of axillary nerve pre and postop.

TABLE 2. Displacement of all lead markers (Pb) between the pre- and postoperative brachial plexus^a

Lead markers	Displacement (mm) Pre – Post plexus
Pb 1	1,20 [§]
Pb 2	1,85 [§]
Pb 3	2,24
Pb 4	3,28
Pb 5	5,62
Pb 6	4,42
Pb 7	7,40
Pb 8	3,73
Pb 9	21,01
Pb 10	35,94
Pb 11	22,67
Pb 12	21,74
Pb 13	21,35
Pb 14	30,30
Pb 15	26,05
Pb 16	25,53

^aPb, lead marker (numbering lead markers see Figure 6A,B). The [§] indicates that the displacement does not exceed the critical level of 1.89 mm, which means that the calculated displacement of the first two markers can be attributed to the error of the measurement procedure with 95% confidence and is ignored. Note the transition between marker 8 and 9.

To the authors' best knowledge there are no reports in literature of detailed 3D models of the brachial plexus reconstructed from CT or MRI scanning. Raphael et al. (2005) produced image-processed 3D volume rendered

magnetic resonance neurography scans, which allow visualization of the brachial plexus within a single composite image; however, this image postprocessing enhancement procedure is not a computerized 3D model and allows no interactive handling.

Cash et al. (2005) presented a reconstruction of the brachial plexus using 3D ultrasound on healthy volunteers. They conclude that their reconstruction is relatively basic only allowing determination of the spatial orientation of the plexus in relation to the first rib and segments of the carotid and subclavian artery. In addition, the quality of that model does not permit detailed labeling as, for example, the divisions and cords could not be distinguished, which consequently means that the model is not suitable for thorough biomechanical measurement.

Lien et al. (2005) introduced a 3D model of the pelvic floor measuring pudendal nerve stretch during vaginal birth. Their protocol of creating the model differs considerably from ours in several ways. First, the pudendal nerve and its branches were dissected profoundly for visualization. Next, the course of the nerves and its orientation toward five landmarks were digitally determined by an optoelectronic digitizing system. The obtained geometric data was scaled and subsequently imported in an already existing published 3D computer model of the pelvic floor and vaginal birth. Each nerve was conceptualized as a homogeneous and stretchable cord and possible nerve fixation points had to be provided to the model for calculation. So, notwithstanding the fact that the information of the nerves is retrieved from cadavers, the model itself is based on several assumptions and integrative manoeuvres. This is in contrast to the current method presented

in this study in which the information building up the model is based on CT images as the only source.

Moreover, in the present study, the nerves are not conceptualized as homogeneous cords but in a more realistic way. The assumption of uniform stretch along the nerves leads to a conservative estimate of nerve strain. In reality, stretch may be greater in certain regions of the nerve depending on their relation with surrounding structures. By dividing the nerves into segments, as in our model, local mechanical differences can be registered. Our results show that the medial (19.3%) and the lateral (15.3%) root of the median nerve are far more strained than other parts of the brachial plexus. These amounts of strain exceed the critical level of 8% known to initiate the arrest of blood flow in the sciatic nerve of rats and rabbits; complete arrest of blood flow will occur at approximately 15% of strain (Lundborg and Rydevik, 1973; Clark et al., 1992). Wall et al. (1992) also showed that nerve conduction was adversely affected by increasing nerve strain: a 12% strain for more than 1 hour resulted in a complete nerve conduction block. This suggests the possibility that "postoperatively" this part of the brachial plexus may be predisposed to nerve injury. However, if for the median nerve the strains found in the different successive segments are expressed in relation to the total length only 3.5% of strain is registered.

The results also show a -10.5% decrease in real length of the postoperative axillary nerve (Table 1). This inevitably means that the preoperative axillary nerve was slightly strained (Fig. 8A) probably as a result of the shoulder being positioned in internal rotation during CT scanning. The strain on the preoperative axillary nerve is illustrated by the lateral course deviation of the proximal radial nerve—as an effect of the axillary nerve pulling—in comparison with the relatively straight course of the postoperative radial nerve (Figs. 3, 4, 5B; here the axillary nerve is behind the humerus). Postoperatively the axillary nerve unwound and relaxed (shortened; Fig. 8B) possibly due to the external rotation of the humerus (Fig. 5C) and distal drop (36 mm) of marker 10' (Fig. 7) at the end of the nerve. Another possible reason for the postoperative shortening may be the fact that marker 10' moved away from the humeral shaft (Fig. 8B), probably as a consequence of releasing and reattaching the deltoid during the insertion of the prosthesis.

If we consider Table 2, showing the displacement of each lead marker, it is obvious that the markers of the distal peripheral nerves moved significantly more relative to the markers of the proximal parts of the brachial plexus, with the transition line between marker 8 and 9 (Table 2). Table 2 also shows that the largest displacement took place around and distal to the shoulder joint. Displacement however was not always proportional to strain. The largest nerve strains were found at the level where the most movement was introduced (distal shift of humerus), which is at the medial and lateral root of the median nerve between markers 8–9 and 6–9 respectively (Table 1, strain; Table 2, displacement; Fig. 7).

At this time, no general conclusions can be drawn based on the biomechanical data, because the number of subjects used is not significant. On the other hand, the results show that the initial purpose is achieved by presenting a method capable of extracting meaningful biomechanical data. This technique can have immediate research applications in studies of nerve biomechanics and for verifying

the anatomical grounds of the neurodynamic tests. The neurodynamic test of the upper limb is a physical technique that is used clinically in diagnosis and treatment of musculoskeletal disorders that show symptoms of a neural component and is better known as the upper limb equivalent of Lasègue's straight leg raise (SLR) test (Keneally et al., 1988; Butler, 2000; Shacklock, 2005).

Because impaired nerve movement becomes increasingly important in the study of specific peripheral neuropathies, there is need to investigate normal nerve dynamics especially in complex regions such as the thoracic outlet. This knowledge may in a later stage serve as a normative database to verify dysfunctional nerve movement in related peripheral neuropathies as, for example, entrapment syndromes and nonspecific arm pain or repetitive strain injury.

The current model can also be applied in further research of the neural consequences of shoulder prostheses (Wirth and Rockwood, 1994; Frankle et al., 2005) as preliminarily performed in the present study. Another potential clinical use of the brachial plexus 3D models is in the field of radiotherapy planning. Radiation-induced brachial plexopathy is a significant cause of morbidity in patients who have received radiotherapy for breast cancer and axillary nodal disease (Olsen et al., 1990, 1993; Johansson et al., 2000; Lim et al., 2007). With the advent of 3D conformal radiotherapy and intensity-modulated radiotherapy, a spatial map of the brachial plexus could be imported into the planning system and the dose to the plexus adjusted accordingly to reduce potential treatment-related adverse effects (Cash et al., 2005). Therefore, it is also crucial to study the location of the brachial plexus as a function of arm position especially "arms up over the head" because this pose is frequently adopted during radiation therapy of the axillary region. Similar studies have already been conducted concerning the target tissues as a result of which is generally accepted that differences in arm position significantly affect the location of axillary lymph nodes (Pergolizzi et al., 2000, 2004; Dijkema et al., 2004; Mansur et al., 2005).

Furthermore, an interactive 3D model of the brachial plexus has the potential to simulate different ways of needle insertion to perform plexus blocks providing anesthesia for shoulder surgery. The use of such models can possibly improve and complete the anesthesiologists' search of safer and more effective approaches (Neal et al., 2002; Feigl et al., 2006; Hopkins, 2007).

There are some limitations in our method that need to be mentioned. Unlike veins and arteries, nerves are not hollow structures and thus the contrast medium cannot fill the whole nerve but has to diffuse around the fibers (Demondion et al., 2005). In some areas, the injection of the mixture went fluently and filled up a lined compartment of the nerve. In other areas of the nerves where an increased injection resistance was perceived, the mixture swelled up into balloon shaped compartments. In fact it is not the plexus itself but rather the distribution of the contrast medium that is reconstructed in 3D.

Stained areas in the surrounding tissue due to leakage of contrast fluid, despite the precautions taken, and local artifacts in the neural tissue caused by scattering of the lead markers were integrated in the reconstruction and had to be manually corrected a posteriori. These manual corrections require a basic understanding of the anatomy of the brachial plexus.

Although minimally invasive, we had to dissect the brachial plexus to reach the different parts with the injection needle and for insertion of the lead markers. Despite the fact that the dissection was performed with maximal preservation of the surrounding attachments of the nerves, it cannot be excluded that this process may have influenced local nerve biomechanics. Neither can it be excluded that the age of the cadaver and the embalming method may have influenced the findings regarding strain and displacement of the nerves.

In the present study, only one side of the specimen was reconstructed and analyzed. Consequently, no general conclusions can be formulated concerning the biomechanical effects of placing a shoulder prosthesis on the brachial plexus.

The results of this study show that the presented method provides the possibility to study the brachial plexus in three dimensional detail in different configurations. The method allows to calculate strain and displacement of the brachial plexus as a function of positional change of the upper limb nerves, in the present study induced by insertion of a reverse shoulder prosthesis.

Currently, the method can be used in vitro for cadaver biomechanical analyses, axillary radiation therapy research (i.e., investigating the exact location of the brachial plexus in "arm up over the head" positions to improve the safety and selectiveness of treatment protocols) and in optimizing the approaches of brachial plexus blocks.

A future aim is to search ways to reconstruct the brachial plexus by means of specialized MRI protocols without the use of contrast fluid. This facilitation will extend the applicability of the model to in vivo studies of normal and abnormal nerve movement, with the objective to improve diagnosis and treatment of peripheral neurogenic disorders.

ACKNOWLEDGMENTS

The authors thank Mr. Aron De Smet for his assistance during the dissection process. We also thank Mr. Pieter Beekman and Mr. Pieter Vandemaele for their help in the reconstruction process of the bones.

LITERATURE CITED

- Allmann KH, Horch R, Uhl M, Gufler H, Althoefer C, Stark GB, Langer M. 1997. MR imaging of the carpal tunnel. *Eur J Radiol* 25:141–145.
- Butler DS. 2000. The sensitive nervous system. 1st ed. Adelaide: Noigroup Publications.
- Cash CJ, Sardesai AM, Berman LH, Herrick MJ, Treece GM, Prager RW, Gee AH. 2005. Spatial mapping of the brachial plexus using three-dimensional ultrasound. *Br J Radiol* 78:1086–1094.
- Clark WL, Trumble TE, Swiontkowski MF, Tencer AF. 1992. Nerve tension and blood flow in a rat model of immediate and delayed repairs. *J Hand Surg [Am]* 17:677–687.
- De Maeseneer M, Jager T, Vanderdood K, Van Roy P, Shahabpour M, Marcelis S. 2003. Ultrasound during dissection of cadaveric specimens: a new method for obtaining ultrasound-anatomic correlations in musculoskeletal radiology. *Eur Radiol* 14:870–874.
- Demondion X, Boutry N, Drizenko A, Paul C, Francke JP, Cotten A. 2000. Thoracic outlet: anatomic correlation with MR imaging. *AJR Am J Roentgenol* 175:417–422.
- Demondion X, Bacqueville E, Paul C, Duquesnoy B, Hachulla E, Cotten A. 2003. Thoracic outlet: assessment with MR imaging in asymptomatic and symptomatic populations. *Radiology* 227:461–468.
- Demondion X, Vidal C, Glaude E, Subocz L, Francke JP, Cotten A. 2005. The posterior lumbar ramus: CT-anatomic correlation and propositions of new sites of infiltration. *AJNR Am J Neuroradiol* 26:706–710.
- Demondion X, Herbinet P, Van Sint Jan S, Boutry N, Chantelot C, Cotten A. 2006. Imaging assessment of thoracic outlet syndrome. *Radiographics* 26:1735–1750.
- Dijkema IM, Hofman P, Raaijmakers CPJ, Legendijk JJ, Battermann JJ, Hillen B. 2004. Loco-regional conformal radiotherapy of the breast: delineation of the regional lymph node clinical target volumes in treatment position. *Radiother Oncol* 71:287–295.
- Dilley A, Greening J, Lynn B, Leary R, Morris V. 2001. The use of cross-correlation analysis between high-frequency ultrasound images to measure longitudinal median nerve movement. *Ultrasound Med Biol* 27:1211–1218.
- Feigl G, Fuchs A, Gries M, Hogan QH, Weninger B, Rosmarin W. 2006. A supraomohyoid plexus block designed to avoid complications. *Surg Radiol Anat* 28:403–408.
- Frankle M, Siegal S, Pupello D, Saleem A, Mighell M, Vasey M. 2005. The Reverse Shoulder Prosthesis for glenohumeral arthritis associated with severe rotator cuff deficiency. A minimum two-years follow-up study of sixty patients. *J Bone Joint Surg Am* 87:1697–1705.
- Greening J, Smart S, Leary R, Hall-Craggs M, O'Higgins P, Lynn B. 1999. Reduced movement of median nerve in carpal tunnel during wrist flexion in patients with non-specific arm pain. *Lancet* 354:217–218.
- Greening J, Lynn B, Leary R, Warren L, O'Higgins P, Hall-Craggs M. 2001. The use of ultrasound imaging to demonstrate reduced movement of the median nerve during wrist flexion in patients with non-specific arm pain. *J Hand Surg [Br]* 26:401–406.
- Hopkins PM. 2007. Editorial. Ultrasound guidance as gold standard in regional anaesthesia. *Br J Anaesth* 98:299–301.
- Hough AD, Moore AP, Jones MP. 2000. Measuring longitudinal nerve motion using ultrasonography. *Man Ther* 5:173–180.
- Hough AD, Moore AP, Jones MP. 2007. Reduced longitudinal excursion of the median nerve in carpal tunnel syndrome. *Arch Phys Med Rehabil* 88:569–576.
- Ide J, Kataoka Y, Yamaga M, Kitamura T, Takagi K. 2003. Compression and stretching of the brachial plexus in thoracic outlet syndrome: correlation between neuroradiographic findings and symptoms and signs produced by provocation manoeuvres. *J Hand Surg [Br]* 28:218–223.
- Johansson S, Svensson H, Denekamp J. 2000. Timescale of evolution of late radiation injury after postoperative radiotherapy of breast cancer patients. *Int J Radiat Oncol Biol Phys* 48:745–750.
- Julius A, Lees R, Dilley A, Lynn B. 2004. Shoulder posture and median nerve sliding. *BMC Musculoskelet Disord* 5:23–29.
- Keneally M, Rubenach H, Elvey R. 1988. The upper limb tension test: the SLR of the arm. In: Grant R, editor. *Physical therapy of the cervical and thoracic spine*. New York: Churchill Livingstone.
- Kleinrensink GJ, Stoeckart R, Vleeming A, Snijders CJ, Mulder PG. 1995. Mechanical tension in the median nerve. The effects of joint positions. *Clin Biomech (Bristol, Avon)* 10:240–244.
- Kleinrensink GJ, Stoeckart R, Mulder PG, Hoek G, Broek T, Vleeming A, Snijders CJ. 2000. Upper limb tension tests as tools in the diagnosis of nerve and plexus lesions. Anatomical and biomechanical aspect. *Clin Biomech (Bristol, Avon)* 15:9–14.
- Lien KC, Morgan DM, Delancey JO, Ashton-Miller JA. 2005. Pudendal nerve stretch during vaginal birth: a 3D computer simulation. *Am J Obstet Gynecol* 192:1669–1676.
- Lim TS, Tetersen V, Zissiadis Y. 2007. CT planning for breast cancer. *Australas Radiol* 51:289–295.
- Lundborg G, Rydevik B. 1973. Effects of stretching the tibial nerve of the rabbit. A preliminary study of the intraneural circulation and the barrier function of the perineurium. *J Bone Joint Surg Br* 55:390–401.
- Mansur DB, Kong F-M, El Naga I, Taylor ME, Zoberi I, Bradley JD, Perez CA, Klein EE. 2005. CT localization of axillary lymph nodes in relation to the humeral head: significance of arm position for radiation therapy planning. *Radiother Oncol* 77:191–193.
- Matsen FA III, Boileau P, Walch G, Gerber C, Bicknell RT. 2007. The reverse total shoulder arthroplasty. *J Bone Joint Surg Am* 89:660–667.
- McLellan DL. 1975. Longitudinal sliding of median nerve during hand movements: a contributory factor in entrapment neuropathy? *Lancet* 1:633–634.

- McLellan DL, Swash M. 1976. Longitudinal sliding of the median nerve during movements of the upper limb. *J Neurol Neurosurg Psychiatry* 39:566–570.
- Millesi H, Zoch G, Rath T. 1990. The gliding apparatus of peripheral nerve and its clinical significance. *Ann Hand Surg* 9:87–97.
- Nakamichi K, Tachibana S. 1995. Restricted motion of the median nerve in carpal tunnel syndrome. *J Hand Surg [Br]* 20:460–464.
- Naraghi R, Hastreiter P, Tomandl B, Bonk A, Huk W, Fahlbusch R. 2004. Three-dimensional visualization of neurovascular relationships in the posterior fossa: technique and clinical application. *J Neurosurg* 100:1025–1035.
- Neal JM, Hebl JR, Gerancher JC, Hogan QH. 2002. Brachial plexus anesthesia: essentials of our current understanding. *Reg Anesth Pain Med* 27:402–428.
- Olsen NK, Pfeiffer P, Mondrup K, Rose C. 1990. Radiation-induced brachial plexus neuropathy in breast cancer patients. *Acta Oncol* 29:885–890.
- Olsen NK, Pfeiffer P, Johannsen L, Schroder H, Rose C. 1993. Radiation-induced brachial plexopathy: neurological follow-up in 161 recurrence-free breast cancer patients. *Int J Radiat Oncol Biol Phys* 26:43–49.
- Pandey SK, Shukla VK. 2007. Anatomical variations of the cords of brachial plexus and the median nerve. *Clin Anat* 20:150–156.
- Pergolizzi S, Settineri N, Gaeta M, Scribano E, Santacaterina A, Ascenti G, Frosina P, De Renzis C. 2000. What is the best position of the arms in mantle field for Hodgkin's disease? *Int J Radiat Oncol Biol Phys* 46:119–122.
- Pergolizzi S, Settineri N, Ascenti G, Blandino A, Santacaterina A, Frosina P, De Renzis C, Di Pasquale A, Gaeta M. 2004. Enlarged axillary nodes and position of the arms in axillary irradiation. *Acta Oncol* 43:182–185.
- Pfirrmann CW, Oberholzer PA, Zanetti M, Boos N, Trudell DJ, Resnick D, Hodler J. 2001. Selective nerve root blocks for the treatment of sciatica: evaluation of injection site and effectiveness. A study with patients and cadavers. *Radiology* 221:704–711.
- Raphael DT, McIntee D, Tsuruda JS, Colletti P, Tatevossian R. 2005. Frontal slab composite magnetic resonance neurography of the brachial plexus: implications for infraclavicular block approaches. *Anesthesiology* 103:1218–1224.
- Shacklock M. 2005. Clinical neurodynamics. A new system of musculoskeletal treatment. 1st ed. Adelaide: Elsevier Butterworth Heinemann.
- Singhal S, Rao VV, Ravindranath R. 2007. Variations in brachial plexus and the relationship of median nerve with the axillary artery: a case report. *J Brachial Plex Peripher Nerve Inj* 2:21.
- Spinner RJ, Edwards PK, Amrami KK. 2006. Application of three-dimensional rendering in joint-related ganglion cysts. *Clin Anat* 19:312–322.
- Swift TR, Nichols FT. 1984. The droopy shoulder syndrome. *Neurology* 34:212–215.
- Thiel W. 1992. The preservation of the whole corpse with natural color. *Ann Anat* 174:185–195.
- Tomandl BF, Hastreiter P, Rezk-Salama C, Engel K, Ertl T, Huk WF, Naraghi R, Ganslandt O, Nimsky C, Eberhardt KEW. 2001. Local and remote visualization techniques for interactive direct volume rendering in neuroradiology. *Radiographics* 21:1561–1572.
- Wall EJ, Massie JB, Kwan MK, Rydevik BL, Myers RR, Garfin SR. 1992. Experimental stretch neuropathy in nerve conduction under tension. *J Bone Joint Surg Br* 74:126–129.
- Wirth MA, Rockwood CA. 1994. Complications of shoulder arthroplasty. *Clin Orthop Relat Res* 307:47–69.
- Wright TW, Glowczewskie F, Wheeler D, Miller G, Cowin D. 1996. Excursion and strain of the median nerve. *J Bone Joint Surg Am* 78:1897–1903.

APPENDIX

Table 3 describes the results of the proximal part of the brachial plexus.

TABLE 3. Real length and vector length of each nerve segment, pre- and postoperatively, determine the biomechanical features for the proximal part of the brachial plexus^a

Nerve segment	v. Length (l_v) (mm)	r. Length (l_r) (mm)	Nerve topology ($l_v - l_r$) / $l_r \times 100\%$	Calculation of strain ($l_{rPost} - l_{rPre}$) / $l_{rPre} \times 100\%$
C5 pre	66.99	69.59	−3.74	2.03
C5 post	67.97	71.01	−4.28	
C6 pre	56.17	60.08	−6.51	−2.26
C6 post	56.61	58.73	−3.61	
C7 pre	61.17	65.13	−6.07	1.54
C7 post	61.98	66.13	−6.28	
C8 pre	63.23	68.19	−7.28	1.03 ^s
C8 post	65.25	68.89	−5.29	
T1 pre	60.81	69.01	−11.89	−0.12 ^s
T1 post	63.11	68.93	−8.44	
ADST pre	40.57	42.45	−4.44	2.52
ADST post	41.29	43.52	−5.12	
ADMT pre	29.45	29.83	−1.27 ^s	3.29
ADMT post	29.97	30.81	−2.74 ^s	
PDST pre	43.53	45.50	−4.32	3.38
PDST post	44.78	47.04	−4.80	
PDMT pre	30.22	32.68	−7.53	−0.98 ^s
PDMT post	31.45	32.36	−2.79	
PDIT pre	21.25	23.57	−9.81	6.73
PDIT post	22.10	25.15	−12.12	
M Cord pre	55.81	59.36	−5.98	1.67
M Cord post	57.14	60.35	−5.31	
L Cord pre	28.09	29.76	−5.60	4.81
L Cord post	29.08	31.19	−6.78	
P Cord pre	34.72	36.75	−5.52	3.64
P Cord post	35.91	38.09	−5.72	

^aThe ratio of the pre- and postoperative real lengths (l_{rPre} and l_{rPost}) determines the amount of strain of a particular nerve segment of the proximal brachial plexus. This percentage interpreted together with the ratio of the real length and the vector length (l_r and l_v) provides information concerning the topology of the nerve segment. pre, preoperative plexus; post, postoperative plexus; v. Length, vector length, shortest distance between both markers demarcating the nerve segment; r. Length, real length measured along the nerve course; Pb, lead marker; C5, root of C5 (ending in Pb 1); C6, root of C6 (ending in Pb 1); C7, root of C7 (ending in Pb 2); C8, root of C8 (ending in Pb 3); T1, root of T1 (ending in Pb 3); ADST, anterior division of the superior trunk (Pb 1–4); ADMT, anterior division of middle trunk (Pb 2–4); PDST, posterior division of superior trunk (Pb 1–5); PDMT, posterior division of middle trunk (Pb 2–5); PDIT, posterior division of inferior trunk (Pb 3–5); M Cord, medial cord (Pb 3–8); L Cord, lateral cord (Pb 4–6); P Cord, posterior cord (Pb 5–7). The ^s indicates that the difference between both lengths does not exceed the critical level of 0.87 mm., which means that it can be attributed to the error of the measurement procedure with 95% confidence.